A Novel Differentially Fed Dual-Polarized Filtering Magneto-Electric Dipole Antenna for 5G Base Station Applications

Dong Yang, Huiqing Zhai®, *Member, IEEE*, Chaozong Guo®, and Chang Ma

Abstract—In this article, a compact differentially fed ±45° dual-polarized filtering magneto-electric (ME) dipole antenna with improved harmonic suppression is proposed and analyzed. First, the fusion of loop-slot dipole and half-wave vibrator is calculated and mentioned to furnish theoretical guidance. Then, by reasonably placing two pairs of second-order step impedance feedlines and a loop-slot patch, a corresponding two-mode loop-vibrator combination filtering antenna with an upper radiation null is naturally constructed. Moreover, simply by loading four open-circuit stubs at the center of octagonal slot patch edge, another extra resonance mode and radiation null in the upper band can be simultaneously obtained. Later, through hiring the reconstructed third-order stub-loaded-resonator (SLR) feedlines, wideband harmonic suppression along with a third radiation null is unaffectedly achieved. Finally, the optimized antenna is fabricated and tested. The measured results reveal it realizes a wideband impedance bandwidth of 42.0% (2.78–4.26 GHz) and a high port isolation of 35 dB. Also, the length of its harmonic suppression is measured from 4.56 to 7 GHz, while the depth reaches more than 20 dB. In addition, the measured gain and radiation efficiency curves in the operating band are relatively stable and both are at a high average value (8.2 dBi, 85%).

Index Terms—Differentially fed, fifth-generation (5G) base station system, filtering antenna, harmonic suppression, slot-vibrator combination.

I. INTRODUCTION

IN RECENT years, mainly owing to its distinctive abilities of balancing average signal level, eliminating multipath, fading, and improving channel capacity, the ±45° dual-polarized antenna has always been a rigid demand for increasingly updated wireless communication systems [1]–[3]. More importantly, with the full-scale approach of the fifth-generation (5G) communication system, issues such as crossband coupling interference and clutter impact caused by the coexistence of multiband base station antenna arrays have been urgently put on the research agenda [4]. Due to the benefits of high

linearity, common-mode rejection, and easy integration, differentially feeding schemes are extra fantastic than single-ended in wireless communication systems. As a result, its derivatives, differentially fed dual-polarized base station antennas with filtering and out-of-band suppression functions, have become a heated topic in the modern communication field.

Specifically, the evolution of a dual-polarized filtering antenna has undergone early independent planning and rigid cascade [5], [6], and finally improved to the current integrated design [7]–[16]. The initial direct series connection often leads to a set of sharp issues, such as impedance mismatch, increased insertion loss, or larger footprint, which seriously deviate from the original intention of a filtering antenna design. Just as the design in [5], only by making a dual-mode stub-loaded-resonator (SLR) couple and tune with a dual-band patch, the antenna can exhibit a wideband second-order filtering feature with a highly harmonic suppression level. However, this application does not obtain even a radiation null to constrain the gain curve.

The current dual-polarized filtering antenna plan tends to cross-use the following manners: slotting, introducing open-circuit branches, adding parasitic patches, loading short-circuit pins, and improving feed networks. Fortunately, such a fusion does not add additional auxiliary structures to harm the integrity of antenna system while maintaining its high efficiency radiation. A typical example, as shown in [10], is that it rarely wraps the half-wave vibrator arm with U-shaped parasitic elements, without affecting its integrality, unexpectedly leading to the generation of two radiation nulls and the widening of working bandwidth. It is a pity that its harmonic suppression bandwidth is significantly insufficient, whose bound less than 13 dB is from 3.6 to 4.0 GHz.

To summarize, although these filtering antennas have made meticulous upgrades on the passband edge selectivity, there is still a lack of means to enlarge the narrow suppression bandwidth outside the operating band. Fortunately, the literature [17]–[19] addresses this serious problem. Basically, they reap the effect of remote electromagnetic wave suppression with the aid of growing the number of radiation nulls outside the high frequency band, which gives us a clue.

Due to the complementarity between electric and magnetic dipoles, magneto-electric (ME) dipole combined antennas are widely used in the dual-polarized base station antenna system. Traditional ME dipole antennas [20]–[22] generally utilize

quarter-wavelength short-circuit vertical panels to equivalent magnetic dipoles instead of adopted loop-slot radiators, which would directly increase the cost of space and materials. Therefore, it is of great practical significance to recombine planar electric vibrators and loop-slot dipole as basic elements into a dual-polarized ME dipole antenna.

In this work, under the exciting of differential-fed signals, a conceptual layout about the mixture of a loop-slot dipole and a pair of half-wave vibrators is first proposed and analyzed. In addition, in the case of different angle phase differences, the loop-vibrator combined radiation patterns without or with the reflector were calculated and demonstrated, which can help provide a theoretical basis for this novel design. Taking this as an opportunity, a compact wideband differentially fed dual-polarized loop-vibrator combined antenna with a second-order harmonic suppression is proposed, which is mainly provided for the 5G base station applications. The stepped impedance feedlines are embedded in the four corners of the dielectric substrate to maintain symmetry and achieve a low cross polarization. With the assistance of an open-circuit stub-loaded octagonal slot patch and four modified feedlines, a three-mode quasi-elliptic function response with three radiation nulls synchronizing can be finally obtained. For verification, a corresponding differential-fed dual-polarized base station antenna of equal proportion is fabricated and tested. Detailed theoretical analysis, measured results, and literature comparison will be presented in detail in the following sections.

II. LOOP-VIBRATOR COMBINED ANTENNA THEORY

The concept of an ME dipole combined antenna was first put forward by Clavin [23] in 1954, which is mainly to obtain the iodized E- and H-plane pattern by concurrently exciting the electric dipole and magnetic dipole. In general, symmetric vibrator and its deformation can be equivalent to the electric dipole, while aperture (wide or narrow gap) or loop slot can be recognized as a magnetic dipole. According to Huygens' principle, if two antenna elements with complementary electrical characteristics and the same polarization orientation are given appropriate feeding conditions, it is possible to obtain a heart-shaped pattern. In view of the fact that loop-vibrator combined antennas are rarely mentioned in the consideration of base station antenna units, this section makes use of the equivalent source idea to derive the +45°-polarized radiation pattern of loop-vibrator dipole combination antenna to supply a foundation for subsequent design.

Fig. 1(a) and (b) shows the concept diagram of +y-[23] and +45°-polarized loop-vibrator ME antenna combination, respectively. As can be seen, apart from the rotation of the axes, the main difference between the two graphs is that the combined antenna shown in Fig. 1(b) utilizes a square slot patch with side length L1 equivalent to the half-wave vibrator, while the feedlines serve to provide phase conversion. Lead the end points A and C of the feedlines into the differential mode excitation. When the vertical junction points B and D between the feedlines and the ring are just at the wave node (short-circuit point), it means the vertical tangent plane connecting the points B and D is magnetic wall and the loop-slot dipole
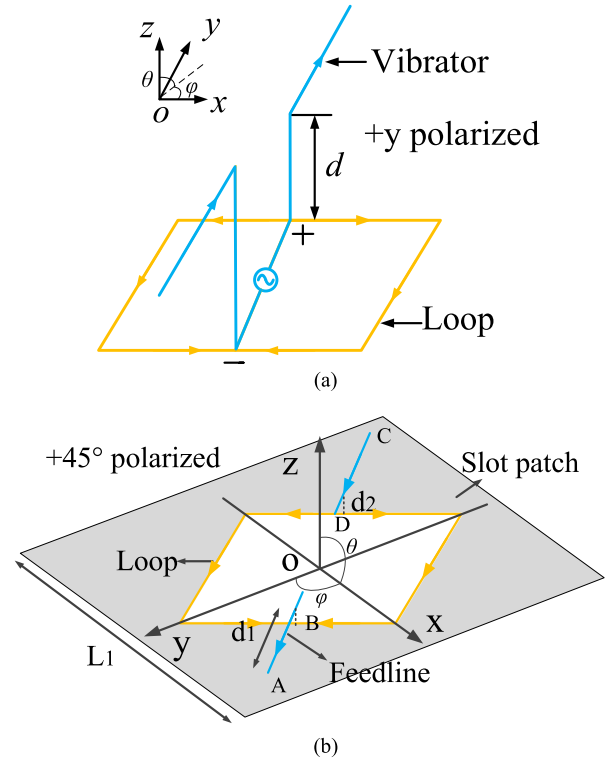

Fig. 1.   Concept diagram of loop-vibrator ME antenna combination. (a) +y polarized. (b) +45° polarized.

can work as even mode [24]. According to the right-hand rule, the magnetic current distribution equivalent to the current distribution of the loop-slot dipole is perpendicular to the current on the feedlines, i.e., the 90° conversion is completed. Since referring to the calculation formula [25] of +y-polarized combined antenna, the calculation results of the normalized radiation electric field of +45°-polarized combined antenna (without metal reflector) are as follows:

$$\vec{E}_{combined-without} = \vec{E}_{45°-loop} + e^{j(kd\cos\theta-\varepsilon)}\vec{E}_{45°-vibrator}$$
$$= \frac{e^{-jkr}}{r}\left[\cos\left(\frac{\pi}{4}\sin\theta\cos\left(\varphi-\frac{\pi}{4}\right)\right)\right.$$
$$\left. + \cos(kd\cos\theta-\varepsilon) + j\sin(kd\cos\theta-\varepsilon)\right]$$
$$* \left(\frac{\vec{\theta}\cos\theta\sin\left(\varphi-\frac{\pi}{4}\right)-}{\vec{\varphi}\cos\left(\varphi-\frac{\pi}{4}\right)}\right). \qquad (1)$$

Here, $\varepsilon = kd$ is the phase delay caused by the distance difference between the half-wave vibrator and the loop-slot dipole. Parameter d is affected by the linear distance d_1 and the height difference d_2 between the vibrator feed port and the loop-slot patch. In order to get the final +45° co-polarization pattern, (1) needs to be converted again by

$$\vec{E}_{45°-polarized}(dB) = 20\lg\frac{\left|E_{\varphi} + E_{\theta}\right|}{\sqrt{2}} \qquad (2)$$

where E_{θ} and E_{φ} represent the vector components at angles θ and φ, respectively. It should be noted that when $\varphi = 0$ (xoz-plane) or $\varphi = \pi/2$ (yoz-plane), their co-polarized patterns are coincident, so only the xoz-plane patterns will be mentioned for simplicity.
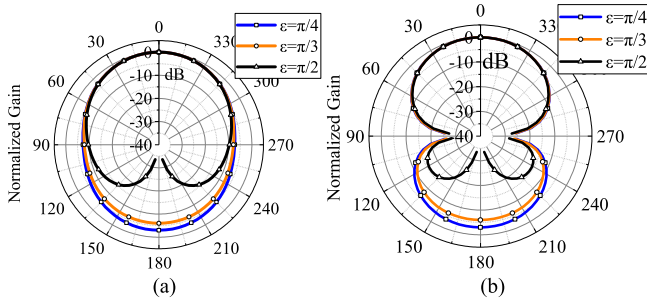
Fig. 2. Normalized radiation pattern in *xoz*-plane ($\varphi = 0$). (a) Without metal ground. (b) With metal ground.

Moreover, (1) does not take into account the effect of metal ground. If an ideal reflector with a quarter wavelength apart is added to the bottom of the structure shown in Fig. 2(b), the overall radiant electric field will be changed into

$$\vec{E}_{combined-with} = 2\sin(kH\cos\theta)\vec{E}_{combined-without}. \quad (3)$$

Then, the auxiliary simulation software MATLAB is utilized to calculate the simulation data of (2) and (3). Fig. 2 shows the normalized radiation pattern in the *xoz*-plane ($\varphi = 0$) with or without a reflector, in which the phase difference is the change factor. As can be observed in Fig. 2(a), with the increase in phase difference ε, the beamwidth of its radiation pattern gradually narrows. When ε is set at $\pi/2$, the Huygens source effect can be produced and the heart-shaped radiation pattern can be naturally obtained. Relatively, the pattern changes with the addition of a metal reflector in a similar way as it does without. The distinction is that the pattern curve gradually converges inward at the two azimuths when θ rotates to 90° and 270°. The above analysis can prove that the phase difference between the loop-slot dipole and half-wave vibrator equals to $\pi/2$ is a more suitable and sensible modeling choice, which can furnish coaching for the following design.

III. DUAL-POLARIZED FILTERING ANTENNA DESIGN

A. Antenna Configuration

Fig. 3 shows the configuration of the proposed differentially fed dual-polarized filtering antenna. As shown in Fig. 3(a) and (c), it mainly consists of a driven slot patch, two pairs of rotating symmetric microstrip feedlines, four 50 Ω coaxial lines, and a copper reflector plate. The microstrip feedline and the driven slot patch are separately fabricated on top and bottom face of a 0.8 mm-thick FR4 dielectric substrate (relative dielectric constant $\varepsilon_r = 4.4$). Meanwhile, the inner conductor of the coaxial line passes through the via hole in the substrate and welds collectively with the end of the upper feedline, while the outer connects to the slot-driven patch. The overall structure uses a copper plate with a thickness of 1 mm as the reflector, with a distance of 23 mm between the FR4 substrate.

As shown in Fig. 3(b), the microstrip feedline is principally composed of three step impedance lines with a pair of open-circuit stubs (stub B) loaded at the middle part. In this setting, the step impedance line is designed to enhance the impedance matching effect of the proposed antenna, and the
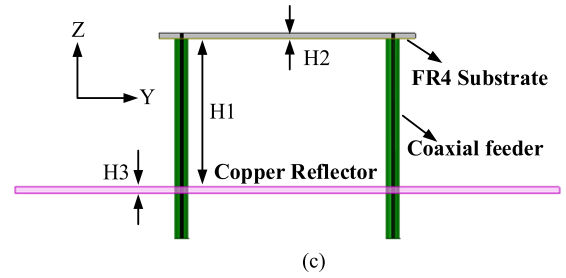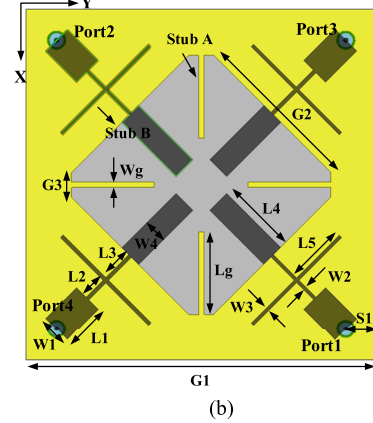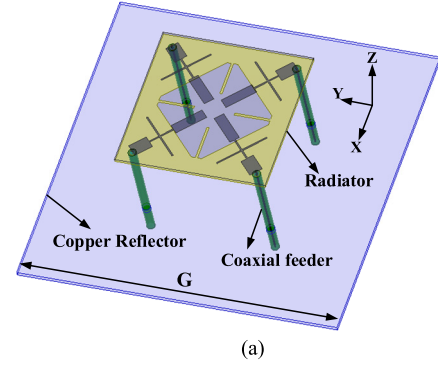

Fig. 3. Configuration of the dual-polarized filtering ME-slot antenna. (a) 3-D view. (b) Top view. (c) Side view. (Relevant parameters: G = 80 mm, G1 = 40 mm, G2 = 18.95 mm, G3 = 2.8 mm, S1 = 3.5 mm, L1 = 5 mm, L2 = 2.75 mm, L3 = 3.73 mm, L4 = 8.72 mm, L5 = 6.9 mm, W1 = 3.65 mm, W2 = 0.4 mm, W3 = 0.4 mm, W4 = 2.7 mm, Lg = 9.45 mm, Wg = 9.45 mm, H1 = 22 mm, H2 = 0.8 mm, and H3 = 1 mm).

open-circuit stub-loading can provide an outside radiation null and substantially improve the upper band suppression level. The driven patch is embedded with unequal-length octagonal slot, and each short side connects to a slender open-circuit stub (stub A) with a size of Lg × Wg. The addition of stub A can simultaneously increase the operating bandwidth by inspiring a new resonant point and improve the roll-off rate along the upper passband edge by generating an approaching radiation null. The end ports of these two pairs of feedlines are named as ports 1–4, respectively. When a pair of differential signals is fed into ports 1 and 2, the proposed filtering antenna achieves +45° polarization radiation. Similarly, when the identical differential signals are fed into ports 3 and 4, the antenna naturally obtains −45° polarization radiation. All the modeling and parameter simulation were carried out by using HFSS19.0, and the finally values after optimization have been shown in the remarks in Fig. 3.
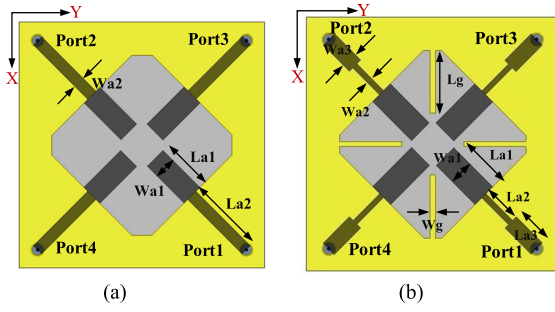
Fig. 4. Top view of the evolved antennas. (a) Ant. I. (La1 = 8.48 mm, La2 = 12.52 mm, Wa1 = 3.63 mm, and Wa2 = 1.89 mm). (b) Ant. II. (La1 = 8.72 mm, La2 = 6 mm, La3 = 6.52 mm, Lg = 9.9 mm, Wa1 = 4 mm, Wa2 = 0.9 mm, Wa3 = 2.5 mm, and Wg = 0.8 mm).
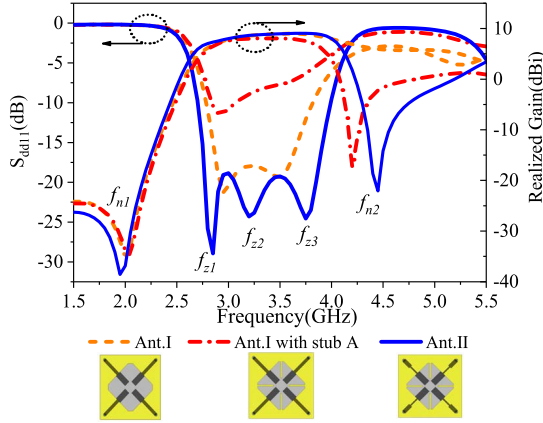

Fig. 5. $|S_{dd11}|$ and realized gain simulated results of three evolved antennas.

B. Working Mechanism

In this section, in order to better describe the design mechanism, Fig. 4 shows two evolved antennas, i.e., antenna I (Ant. I) and antenna II (Ant. II) with their corresponding dimensions, and Fig. 5 shows the simulation results of the corresponding reflection coefficient and peak realized gain. For the comfort of assessment, the results of transitional antenna (Ant. I with stub A) are also provided, and besides the adjustment of the feedline, other parameters remain unchanged.

They will be dissected and narrated below.

1) Reference Ant. I: With reference to Fig. 4(a), Ant. I is the basis differentially fed dual-polarized ME dipole combined antenna, which consists of two pairs of symmetrical second-order step impedance feedlines and a loop-slot radiator. It can be clearly observed that Ant. I has two resonant points f_{z1}(2.95 GHz) and f_{z2}(3.5 GHz) alongside a radiation null f_{n1} (2 GHz), and its impedance relative bandwidth ($|S_{dd11}|$ < −15 dB) can reach 24.66% (2.88–3.69 GHz). As for the realized gain curves, with the assistance of null f_{n1}, Ant. I realizes a notably declined roll-off rate at upper passband edge and conversely slowly on the other side.

Fig. 6(a) and (b) shows the E-field (in $\phi = 45°$ plane) and surface current distribution of Ant. I at the corresponding resonant point f_{z1}(2.95 GHz), while Fig. 6(c) and (d) shows the H-field (in $\phi = -45°$ plane) and surface current distribution at resonant point f_{z2}(3.5 GHz). In this setting, only the two ports (ports 1 and 2) toward the +45°-polarized direction are input with equal amplitude reverse excitation signals, while
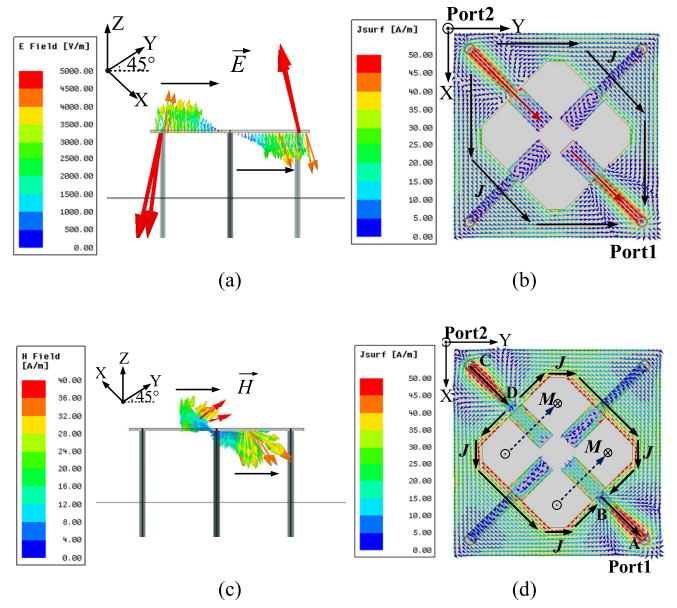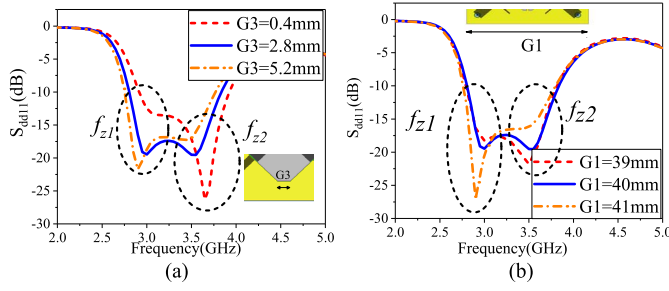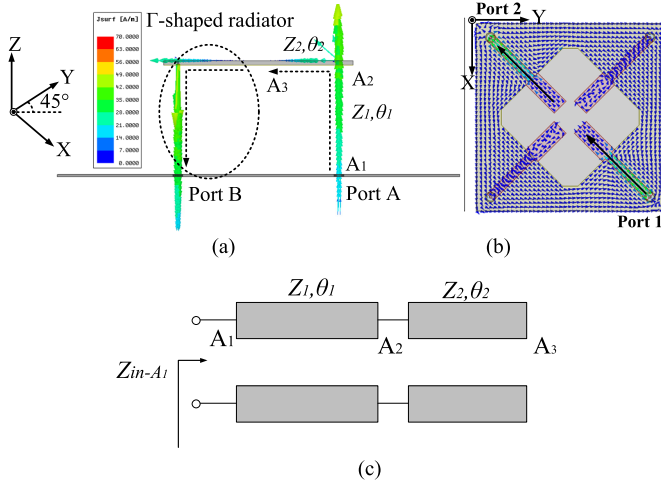

Fig. 6. E-field and surface current distribution of Ant. I at 2.95 GHz. (a) E-field distribution in $\phi = 45°$ plane. (b) Surface current distribution. H-field and surface current distribution of Ant. I at 3.5 GHz. (c) H-field distribution in $\phi = -45°$ plane. (d) Surface current distribution.

the other two are given impedance matching. As shown in Fig. 6(a), the indicating line of E-field (in $\phi = 45°$ plane) completes a transition from the crest to the trough and then to the crest, which is equivalent to the completion of a one-half cycle. The surface current distribution in Fig. 6(b) also shows that the surface current flows from one vertex of the slot patch to the other along +45°-polarized direction. Meanwhile, the diagonal length of the driven slot patch ($\sqrt{2}$ G1 = 56.6 mm) is about one-half wavelength (50.8 mm) corresponding to the lower resonant point (2.95 GHz). Therefore, the slot patch assumes the role of a half-wavelength electric dipole (+45°-polarized) at 2.95 GHz. It can be actually seen from Fig. 6(c) that the directions of the H-field along $\phi = -45°$ direction at 3.5 GHz are reversed, which coincides with the magnetic field equivalent to the current distribution along the octagon slot (right-hand rule) in Fig. 6(d). Here, the octagon slot will act as magnetic dipoles (−45° polarized) and its half-circle circumference (2 × G2 + 2 × G3 = 43.5 mm) approximates to one-half wavelength (42.9 mm) of higher resonant point (3.5 GHz). It is worth noting that Ant. I uses channel A→B and channel C→D to provide differential signals and complete a 90° phase conversion. Moreover, the current at two points B and D (intersection point of step impedance feedline) is at the wave node of the resonance period corresponding to point f_{z2} and is equivalent to a short circuit here. In sum, Ant. I works as a combination of electric dipoles (+45° direction) and magnetic dipoles (−45° direction) in the operating band.

To assist in analyzing the effect of loop-vibrator dipole on the position of points f_{z1} and f_{z2} of Ant. I, Fig. 7(a) and (b) shows the simulated reflection coefficient results changing by two important parameters G3 (the length of short side of octagonal slot) and G1 (the side length of the slot patch), respectively. As shown in Fig. 7(a), the resonance point f_{z2} is more sensitive to the change of G3 than point f_{z1}, and

Fig. 7. Simulated $|S_{dd11}|$ of Ant. I change by different (a) G3 and (b) G1.

Fig. 8. (a) Surface current distribution on inner conductor of the coaxial cables and the stepped impedance feedline at radiation null f_{n1} along +45° polarization direction. (b) Current distribution on the top surface at radiation null f_{n1}. (c) Equivalent circuit at feeding point A.

its position moves toward low frequency with the increase of G3. It happens to verify that the octagonal slot plays a key role in the generation of resonance point f_{z2}. When referring to Fig. 7(b), as G1 raises, the position of point f_{z1} is closer to a low frequency, while point f_{z2} hardly moves. It directly reveals that resonance point f_{z1} is produced by the slot patch. It is worth noting that these two resonant points can be independently controlled by the octagonal loop and the slot patch, which allows Ant. I to obtain a dual-mode passband by adjusting the size appropriately.

As seen in Fig. 5, Ant. I has a significant upper edge radiation null f_{n1} at 2 GHz, and it helps improve the roll-off rate along the left passband. To apprehend its birth, Fig. 8(a) shows the surface current distribution on inner conductor of the coaxial cables and the stepped impedance feedline along the +45°-polarized direction, while Fig. 8(b) shows the top surface current distribution at radiation null f_{n1}. It can be clearly viewed that the current concentrated on a single Γ-shaped radiator forms a quarter-period loop and little energy can be transferred to the slot patch, which leads Ant. I to not radiate properly. To aid analysis, Fig. 8(c) shows the equivalent circuit at feeding point A. Here, points A and B correspond to the starting points of the coaxial feed inner core of ports 1 and 2, while (Z_1, θ_1) and (Z_2, θ_2) represent the input impedance and equivalent electrical length of the inner conductor of the coaxial cables and the electric dipole arm, respectively. Points A1, A2, and A3 can be regarded as three
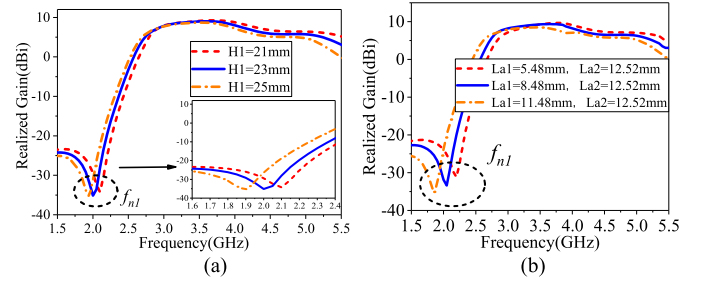
Fig. 9. Simulated realized gain curves of Ant. I change by different (a) H1 and (b) La1 + La2.

nodes in the equivalent circuit. Then, the input impedance Z_{in-A1} of the circuit can be derived as

$$
\begin{aligned}
Z_{in-A1} &= Z_1 \frac{Z_{in-A2} + jZ_1 \tan \theta_1}{Z_1 + jZ_{in-A2} \tan \theta_1} \\
&= Z_1 \frac{-jZ_2 + jZ_1 \tan(\theta_1) \tan(\theta_2)}{Z_1 \tan(\theta_2) + Z_2 \tan(\theta_1)}.
\end{aligned} \tag{4}
$$

When Ant. I, shown in Fig. 8(a), resonates at point 2 GHz, the input impedance Z_{in-A1} approaches infinity. In this case, according to transmission line theory [26], when the equivalent sum of electrical length θ_1 and the electrical length θ_2 in series is equal to $\pi/2$, the input impedance Z_{in-A3} transmitted from points A1–A3 can become zero, and then will be seriously mismatched with the original open-circuit status at the right end. Almost all of the energy is reflected back, thus exciting a radiation null f_{n1}. From the above analysis, the position of null f_{n1} can be determined by the length of the inner conductor of the coaxial cables (H1) and the stepped impedance feedline (La1 + La2), i.e., its position can be estimated by

$$
f_{n1} \approx \frac{c}{4H_1 + 4La_1 + 4La_2}. \tag{5}
$$

To further present the effects of parameters H1 and La1 + La2 on the position of radiation null f_{n1} of Ant. I, Fig. 9 shows the simulated realized gain curves change by these variables. As shown in Fig. 9(a), with the enlarging of parameter H1 from 21 to 25 mm, the position of null f_{n1} shifts downward from 2.1 GHz to a lower frequency 1.9 GHz. A similar trend is also seen in Fig. 9(b); with parameter La1 + La2 raising from 18 to 24 mm, the position of null f_{n1} decreases from 2.17 to 1.84 GHz. Unsurprisingly, their reactions are consistent with the rules derived from (5).

2) Reference Ant. II: In order to expand the working bandwidth and introduce the upper band filtering functions, four extra open stubs (stub A) are etched on the center of the short side of octagonal slot and the step-impedance feedline are reorganized from two to three steps, and thus switching from Ant. I to Ant. II. It can be seen in Fig. 5 that a new upper-band radiation null f_{n2} can be generated simply by adding stub A to Ant. I, but this modification has seriously affected its impedance matching, and the average reflection coefficient $|S_{dd11}|$ within band (2.88–3.69 GHz) has been lowered by nearly 10 dB overall. Relative to Ant. I with stub A, Ant. II is adjusted with the step-impedance feedline from second order to third order. Such a refinement eventually makes Ant. II realizes a wider operating band from 2.75 to
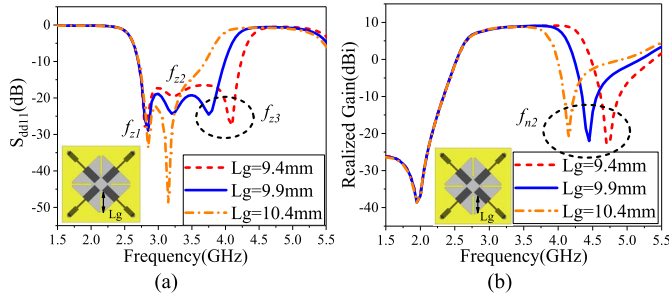
Fig. 10.   Simulated $|S_{dd11}|$ and realized gain curves of Ant. II change by different Lg (a) $|S_{dd11}|$. (b) Realized gain.
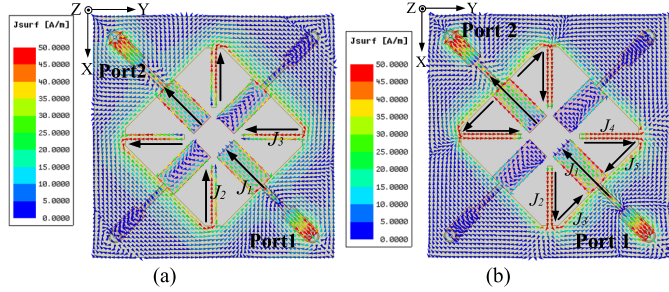

Fig. 11.   Current distributions on Ant. II at (a) resonant point f_{n3} and (b) radiation null f_{n2}.

3.92 GHz with three resonant modes (f_{z1}, f_{z2}, and f_{z3}). Moreover, the realized gain at the broadside direction ($\theta = 0°$) within passband becomes even flatter and has an average of 10 dBi. Aiming to better make clear the length of stub A (Lg) on the influence of resonance point f_{z3} and radiation null f_{n2}, Fig. 10 shows the simulated $|S_{dd11}|$ and realized gain results of Ant. II changing by different Lg. As observed in Fig. 10(a), when parameter Lg varies from 9.4 to 10.4 mm with a step of 0.5 mm, the resonance point f_{z3} changes obviously and gradually transfer to low frequency as it grows and further compress the operating bandwidth, while the other two resonance points f_{z1} and f_{z2} barely move with little influenced. As for radiation null f_{n2}, it keeps a comparable trajectory with point f_{z3}, i.e., an inversely proportional trend to the increase in frequency. Moreover, its presence will only affect the upper outside filtering effect, no longer the lower. Note that Lg = 9.9 mm is ultimately chosen to maintain an appropriate bandpass performance. According to reference [27], the location of transmission zeros in filter can be decided by the equivalent electrical length (θ) of the grafted open stubs by setting $\theta = \pi/2$. Surely, it can be applied analogically to the extraction of radiation null f_{n2}. Finally, null f_{n2} can be finally achieved as

$$f_{n2} = \frac{c}{4\sqrt{\varepsilon}Lg}. \tag{6}$$

It is rather unfortunate that the level of distal out-of-band suppression does not improve overall and is raised to a certain extent. Thankfully, this problem will be solved in the design of Ant. III. For further penetration analysis, Fig. 11(a) and (b) shows the surface current distribution of Ant. II at resonant point f_{n3} (3.75 GHz) and radiation null f_{n2} (4.45 GHz). Considering the central symmetry of the structure,
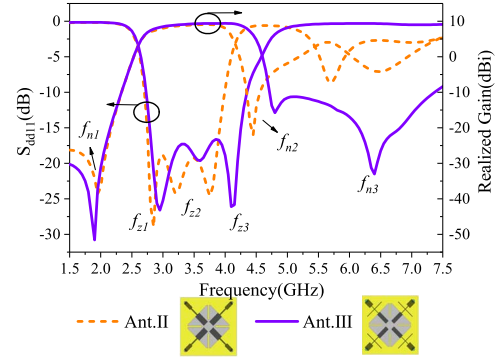

Fig. 12.   Simulated $|S_{dd11}|$ and realized gain curves of Ant. II and Ant. III.

the current distribution of the lower right quarter module will be analyzed emphatically. As depicted, the black arrows in the figure represent the main direction of current. In Fig. 11(a), the vector total of the current on the open-circuit stub ($J_1 + J_2$) has the same $+45°$ polarization direction as the current (J_3) on the third-order feedlines at point f_{z3}, which contributes to the gain superposition and bandwidth enhancement. On the contrary, in Fig. 11(b), the current J_1 on the feedlines has the same magnitude and opposite phase with the current vector sum ($J_1 + J_2 + J_4 + J_5$) nearby, thus achieving a kind of mutual cancellation. It eventually leads to the creation of a new null point f_{n3} in the far-region radiation field.

3) Reference Ant. III: To further deal with the remaining problem about a lower upper-band suppression level, the feedline of Ant. II is slightly tuned with adding a pair of open-circuit stub (stub B) on the thinnest impedance line, and finally it evolves into Ant. III. Moreover, Fig. 12 shows the simulated $|S_{dd11}|$ and realized gain results between Ant. II and Ant. III to compare its transformation. It can be found that the development not only helps Ant. III achieve a wider operating bandwidth 42.4% from 2.79 to 4.29 GHz with $|S_{dd11}| < -15$ dB, but also introduce an extra radiation null f_{n3} to suppress the far-end stray response. Similar to the traditional design technique of normal SLR, Ant. III places a pair of branches at the symmetry axis of its second step-impedance feedline to form a symmetric structure. This combination may operates as a low-pass filter without destroying its in-band radiation, and then emerges a quasi-elliptic bandpass response. Using the average gain of 10 dB in the passband as a reference, the suppression level of Ant. III outside the upper band can reach 20 dB from 4.70 to 7.45 GHz.

To state the effects of stub B on the position of radiation null f_{n3}, the simulated realized gain curves changing by relevant parameters L5 (the length of stub B) and L2 (the distance from the first step impedance line connecting port 1 to stub B) are studied and shown in Fig. 13. When the length of parameters L5 and L2 are both adjusted, the gain curve is only sensitive to the former, which is shown as radiation null f_{n3}. These two contrasts deeply reveal that the location of null f_{n3} will be directly determined by the length of stub B. Therefore, null f_{n3} can be estimated by
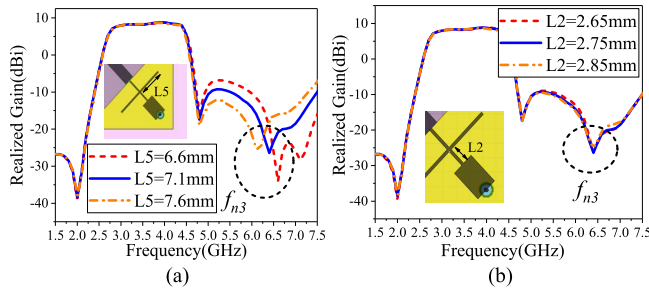
$$f_{n3} = \frac{c}{4\sqrt{\varepsilon}L5}. \tag{7}$$

Fig. 13. Simulated gain curves of Ant. III change by different (a) L5 and (b) L2.
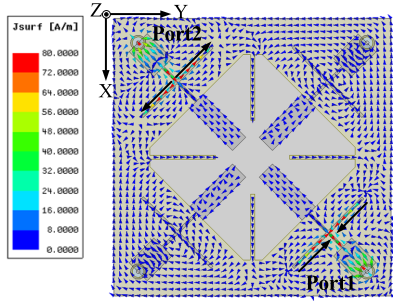

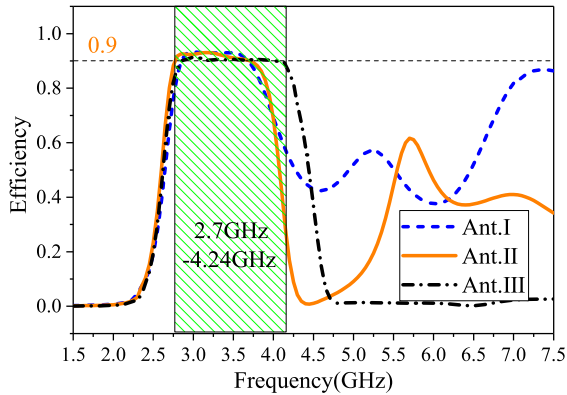Fig. 14. Current distribution on Ant. III at radiation null f_{n3}.

Fig. 15. Simulated radiation efficiency results from Ant. I to Ant. III.
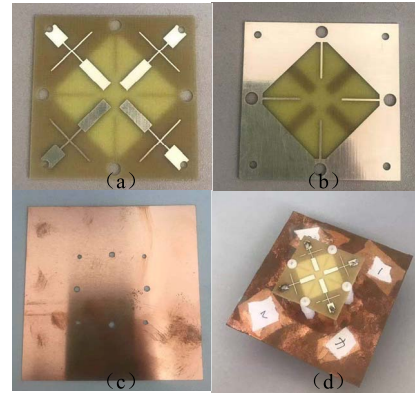

Fig. 16. Photograph of the fabricated antenna. (a) Front view of the upper dielectric substrate. (b) Bottom view of the upper dielectric substrate. (c) Metal reflector. (d) 3-D view.
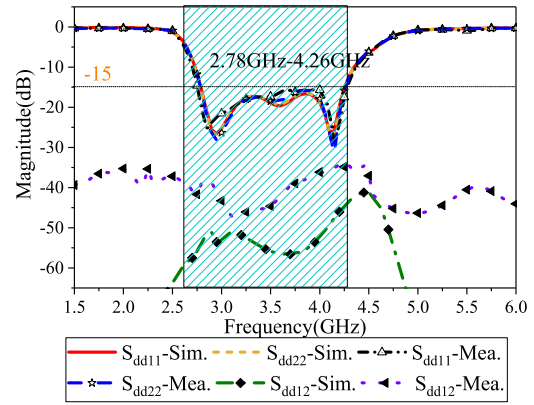

Fig. 17. Simulated and measured *S*-parameter magnitudes of Ant. III.

the above analysis, the reasonable structure allocation in this section makes Ant. III not only own efficient in-band radiation response, but also possess out-of-band filtering and harmonic suppression characteristics. Naturally, the design of Ant. III can be applied to multifunctional communication systems.

IV. EXPERIMENTAL RESULTS

Based on the optimized size specifications, Ant. III was finally manufactured and tested, and Fig. 16 shows a variety of view photographs of the fabricated antenna. Here, it utilizes an Agilent N8722ES network analyzer to measure its *S*-parameter values and a near-field Satimo StarLab system for its realized gains, efficiencies, and radiation patterns. When dealing with the conversion from one input port to two differential ports, a 180° coupling hybrid (TBG-2080-35-180) is employed. Fig. 17 shows the simulated and measured *S*-parameter magnitudes of Ant. III. It should to be stated that the measured *S*-parameter values (*Sij*, *i*, *j* = 1–4) are original and unprocessed. After being transformed by formulas provided in literature [20], the differential mode reflection coefficients (S_{dd11}, S_{dd22}) and isolation (S_{dd12}) can be naturally obtained. It is clearly observed that the overlapping part of the slash shadow that stands for proper functioning ($|S_{dd11}|$ and $|S_{dd22}| < -15$ dB) can range from 2.78 to 4.26 GHz, which can completely cover 5G N77 communication bands. The simulated and measured isolation $|S_{dd12}|$ within the entire operating band are both lower than −35 dB, mainly resulting

The surface current distribution on Ant. III at radiation null f_{n3} is shown in Fig. 14. It can easily be learned that the signals excited from ports 1 and 2 at the +45°-polarized direction are almost all blocked by the open-circuit stub B, and little energy is transmitted to the far end to resonate with the slot magnetic dipole. The currents at stub B cancel each other out, resulting in a new radiation null f_{n3} generating.

It ought to be noted that no extra complexity is added to affect the integrity of the final antenna as it evolves from Ant. I to Ant. III. The simulated radiation efficiency curves from Ant. I to Ant. III at the boresight direction ($\theta = 0°$) are shown in Fig. 15. It can be virtually considered that the radiation efficiency of these three antennas can reach more than 90% in their respective operating bands. In addition, their efficiency curves are close to zero below 2.3 GHz, which mainly results from the existence of radiation null f_{n1}. On the contrary, due to the constraints of nulls f_{n1} and f_{n2}, Ant. III shows a better second-order harmonic suppression level outside the upper passband than Ant. I and Ant. II. Based on
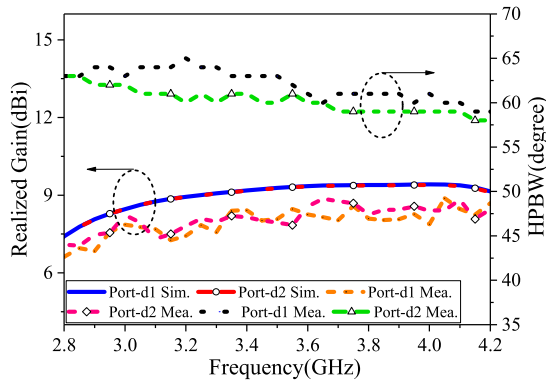
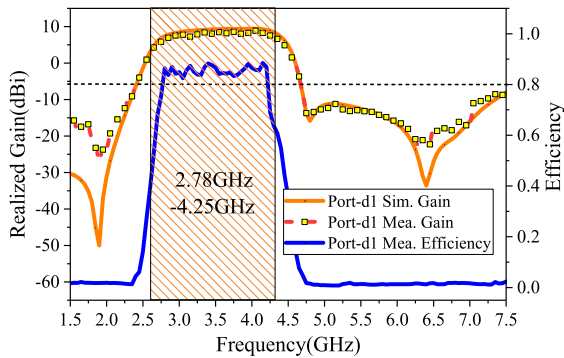Fig. 18. Realized gains and HPBWs of Ant. III.

Fig. 19. Realized gains and efficiency of Ant. III as differential port-d1 is excited.

from differential excitation settings. The measured gain result in this target range in Fig. 18 shows that its average is close to 8.2 dBi, nearly 1 dB less than the simulated. The obvious deviation may be caused by the insertion loss caused by the test cable and machining error. Meanwhile, the measured stable half-power beamwidths (HPBWs) between ports-d1 and d2 reaches $60° \pm 3°$. For simplification, only $+45°$-polarized ports are excited, and the gains and efficiency results of Ant. III are shown in Fig. 19. As observed, both the upper and lower passband edges present a steep roll drop with out-of-band inhibition level more than 20 dB, including 1.8–2.28 GHz and 4.73–7 GHz. Within the suppression frequency band, the measured radiation efficiency can approach zero, but on the contrary, it exhibits an in-band (2.78–4.25 GHz) average value greater than 0.85.

Fig. 20 shows the measured and simulated normalized E-plane (Phi = 0°) and H-plane (Phi = 90°) radiation patterns when differential port-d1 is excited at 2.95, 3.6, and 4.1 GHz. Across the whole mentioned curves, the proposed antenna has a stable unidirectional broadside radiation patterns.

As expected, the measured and simulated co-polarization curve trajectories ($+45°$ polarized) are similar to the direction diagram calculated above, which confirms the correctness of the design concept. In the broadside direction, both E-plane and H-plane radiation patterns within these three points hold a degree of isolation greater than 30 dB between co- and cross-polarization.

A specific comparison between this filtering antenna and different associated ones about some primary indications is summarized in Table I. When particular to each case, the
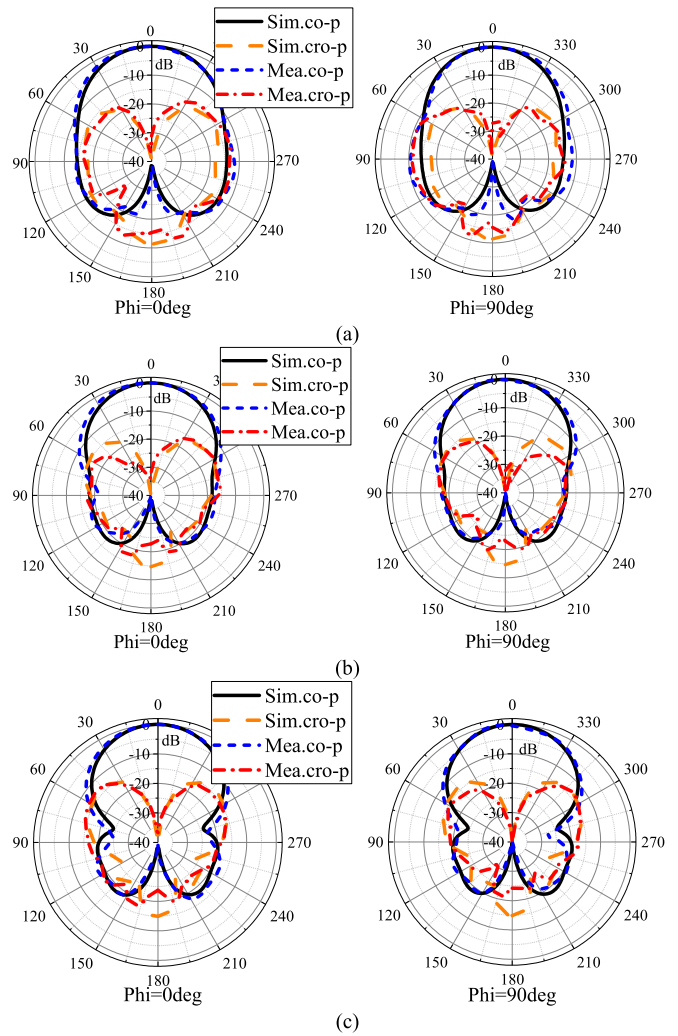

Fig. 20. Normalized E-plane (left) and H-plane (right) radiation patterns of the proposed filtering antenna when port-d1 is excited at (a) 2.95, (b) 3.6, and (c) 4.1 GHz.

design in [7] presents a superb layout for a dual-polarized base station filtering antenna that consists of the benefits of miniaturization, high isolation, and excessive out-of-band suppression levels. But it still suffers from too many layers and insufficient bandwidth (only 12.2%). Furthermore, it can be effortlessly patrolled that the antennas in [9]–[11], and [17] are ordinarily supplied for 2G/3G/4G (1.7–2.7 GHz) base station purposes which have a wider working bandwidth than others. However, the suppression capabilities of the designs in [9]–[11] are insufficient in depth and breadth, which may be regarded as a rigid flaw for filtering antennas. Although the work in [17] performs well under most standards, its average in-band gain is a bit low, and its dual-polarization modes are more precisely 0° and 90° polarized, which is not required for conventional base station antennas. In contrast with comparable relevant communication systems (3.3–4.2 GHz for 5G), the proposed antenna has a wider impedance bandwidth, an incredible port isolation, and a deeper level of harmonic suppression than related contents in [12], [13], [15], and [16]. It is worth noting that the antenna in [16] is also an ME dipole combined antenna. Although it has lifted the

TABLE I
COMPARISON WITH SIMILAR DUAL-POLARIZED FILTERING ANTENNAS

Ref.	Feeding type	Dual polarization modes	Nu. of nulls /resonances	Height (λ_0)	Overall/ Radiator size (λ_0^2)	Ave.gain (dBi)	Bandwidth	Isolation (dB)	Rejection Level (dB)	Bandwidth of HS
[7]	Single -ended	0°/90°	2/2	0.13	0.75×0.75/ 0.27×0.27	9	12.2%(2.46-2.78GHz) $|S_{11}| < $-15dB	> 35	21.5	Without
[9]	Single -ended	±45°	2/-	0.23	1.03×1.03/ 0.37×0.37	8.15	52.2%(1.6-2.73GHz) VSWR < 1.5	> 34	17	Without
[10]	Single -ended	±45°	2/3	0.26	0.98×0.98/ 0.41×0.41	8.5	63%(1.68-3.23GHz) VSWR < 1.5	> 34	13	Without
[11]	Single -ended	±45°	3/2	0.22	-/ 0.48×0.48	8	48.8%(1.7-2.8GHz) $|S_{11}| < $-10dB	> 35	13	Without
[12]	Single -ended	±45°	-/-	0.14	0.53×0.72/ 0.31×0.31	8.1	25%(3.3-4.2GHz) $|S_{11}| < $-10dB	> 25	20	2.4fc
[13]	Differential -fed	±45°	2/-	0.13	0.75×0.75/ 0.31×0.31 @3.5GHz	8.34/8.7	12.3%(3.28–3.71GHz) 7.6%(4.8–5.18GHz) VSWR < 1.5	> 37/ > 38	17.7	Without
[15]	Single -ended	±45°	3/3	0.11	0.75×0.75/ 0.44×0.44	8.2	27.6%(3.3-4.36GHz) $|S_{11}| < $-15dB	> 25	20	Without
[16]	Differential -fed	±45°	-/3	0.15	0.7×0.7/ 0.45×0.45	8.1	22.2%(3.12-3.9GHz) VSWR < 1.5	> 35.2	18.5	Without
[17]	Differential fed	0°/90°	4/3	0.25	1.05×1.05/ 0.38×0.38	7.55	49%(1.7-2.81GHz) $|S_{dd11}| < $-15dB	> 39	12.65	4fc
[18]	Single -ended	±45°	-/3	0.21	1.05×1.05/ 0.58×0.58	7.5	35.2%(680-970MHz) $|S_{11}| < $-15dB	> 35	13.8	4.6fc
[19]	Differential -fed	0°/90°	2/3	0.083	0.6×0.6/ 0.37×0.37	7.9	15%(2.35-2.7GHz) $|S_{dd11}| < $-10dB	> 30	13	2.6fc
Pro.	Differential -fed	±45°	3/3	0.25	0.94×0.94/ 0.47×0.47	8.2	42.0%(2.78-4.26GHz) $|S_{dd11}| < $-15dB	> 35	20	2fc

Nu. of nulls /resonances are the number of radiation nulls and resonance points. Bandwidth of HS: Bandwidth of harmonic suppression. fc: center frequency.

restriction of profile height and performed exceptional in-band radiation and out-of-band filtering response with the aid of improved feedlines and slit technology, its suppression cutoff line is solely up to 5 GHz, which is a little short. The designs in [18] and [19] do well in this part that their suppression tipping points can reach 4.6 times [18] and 2.6 times [19] relative to the center frequency. However, they both have their personal drawbacks as the antenna in [18] does not mention the low-frequency-filtering feature and the antenna in [19] does not meet the index of a base station antenna unit.

In generally, the proposed filtering antenna has a greater comprehensive performance in these several indicators, such as wide operating bandwidth, high isolation, high out-of-band rejection level, and wideband harmonic suppression, which states the potential to be applied to practical application.

V. CONCLUSION

In this article, a novel differentially fed ±45° dual-polarized ME dipole filtering antenna with a wideband harmonic suppression is proposed. First, the combination of loop-slot dipole and half-wave vibrator is formulated and analyzed. By assigning a phase difference of 90° to the two electrically complementary antenna elements, the cardiac radiation pattern can be naturally obtained. Moreover, open-circuit slot stubs and

third-order SLR feedlines are introduced to expand bandwidth and enhance filtering performance. Without adding an extra filtering circuit, a three-resonant passband with three radiation nulls is correctly inspired. Finally, the antenna prototype was processed and tested for verification. The measured results point out that it possesses a wide impedance bandwidth of 27.6% (2.78–4.26 GHz for $\|S_{dd11}\| > 15$ dB) and a high port isolation of 35 dB. Also, in the whole passband, it has a stable gain curve with an average of 8.2 dBi and a low oscillating radiation efficiency over 85%. The rejection level is more than 20 dB within the lower stopband of 1.5–2.3 GHz and the upper stopband band of 4.72–7 GHz. In conclusion, when confronted with increasingly complicated electromagnetic environments, the presented filtering antenna is an incredible alternative suitable for 5G communication systems.

REFERENCES

[1] Y. Cui, R. Li, and H. Fu, "A broadband dual-polarized planar antenna for 2G/3G/LTE base stations," *IEEE Trans. Antennas Propag.*, vol. 62, no. 9, pp. 4836–4840, Sep. 2014.

[2] Y. Gou, S. Yang, J. Li, and Z. Nie, "A compact dual-polarized printed dipole antenna with high isolation for wideband base station applications," *IEEE Trans. Antennas Propag.*, vol. 62, no. 8, pp. 4392–4395, Aug. 2014.

[3] H. Huang, Y. Liu, and S. Gong, "A broadband dual-polarized base station antenna with sturdy construction," *IEEE Antennas Wireless Propag. Lett.*, vol. 16, pp. 665–668, 2017.

[4] H. Huang, X. Li, and Y. Liu, "A low-profile, dual-polarized patch antenna for 5G MIMO application," *IEEE Trans. Antennas Propag.*, vol. 67, no. 2, pp. 1275–1279, Feb. 2019.

[5] C.-X. Mao, S. Gao, Y. Wang, F. Qin, and Q.-X. Chu, "Multimode resonator-fed dual-polarized antenna array with enhanced bandwidth and selectivity," *IEEE Trans. Antennas Propag.*, vol. 63, no. 12, pp. 5492–5499, Dec. 2015.

[6] C.-X. Mao, S. Gao, Y. Wang, Q. Luo, and Q.-X. Chu, "A shared-aperture dual-band dual-polarized filtering-antenna-array with improved frequency response," *IEEE Trans. Antennas Propag.*, vol. 65, no. 4, pp. 1836–1844, Apr. 2017.

[7] W. Duan, X. Y. Zhang, Y.-M. Pan, J.-X. Xu, and Q. Xue, "Dual-polarized filtering antenna with high selectivity and low cross polarization," *IEEE Trans. Antennas Propag.*, vol. 64, no. 10, pp. 4188–4196, Oct. 2016.

[8] Y. Zhang, X. Y. Zhang, L. Gao, Y. Gao, and Q. H. Liu, "A two-port microwave component with dual-polarized filtering antenna and single-band bandpass filter operations," *IEEE Trans. Antennas Propag.*, vol. 67, no. 8, pp. 5590–5601, Aug. 2019.

[9] C. F. Ding, X. Y. Zhang, Y. Zhang, Y. M. Pan, and Q. Xue, "Compact broadband dual-polarized filtering dipole antenna with high selectivity for base-station applications," *IEEE Trans. Antennas Propag.*, vol. 66, no. 11, pp. 5747–5756, Nov. 2018.

[10] C. F. Ding, X. Y. Zhang, and M. Yu, "Simple dual-polarized filtering antenna with enhanced bandwidth for base station applications," *IEEE Trans. Antennas Propag.*, vol. 68, no. 6, pp. 4354–4361, Jun. 2020.

[11] Y. F. Cao, Y. F. Wu, Y.-M. Pan, and X. Y. Zhang, "A method of generating radiation nulls utilizing inherent resonance modes for dual-polarized filtering dipole antenna design," *IEEE Trans. Antennas Propag.*, vol. 68, no. 8, pp. 6413–6418, Aug. 2020.

[12] S. J. Yang, Y. F. Cao, Y. M. Pan, Y. Wu, H. Hu, and X. Y. Zhang, "Balun-fed dual-polarized broadband filtering antenna without extra filtering structure," *IEEE Antennas Wireless Propag. Lett.*, vol. 19, no. 4, pp. 656–660, Apr. 2020.

[13] Y. Li, Z. Zhao, Z. Tang, and Y. Yin, "Differentially fed, dual-band dual-polarized filtering antenna with high selectivity for 5G sub-6 GHz base station applications," *IEEE Trans. Antennas Propag.*, vol. 68, no. 4, pp. 3231–3236, Apr. 2020.

[14] K. Xue, D. Yang, C. Z. Guo, H. Q. Zhai, H. K. Li, and Y. Zeng, "A dual-polarized filtering base-station antenna with compact size for 5G applications," *IEEE Antennas Wireless Propag. Lett.*, vol. 19, no. 8, pp. 1316–1320, Aug. 2020.

[15] S. J. Yang, Y. M. Pan, Y. Zhang, Y. Gao, and X. Y. Zhang, "Low-profile dual-polarized filtering magneto-electric dipole antenna for 5G applications," *IEEE Trans. Antennas Propag.*, vol. 67, no. 10, pp. 6235–6243, Oct. 2019.

[16] Y. Li, Z. Zhao, Z. Tang, and Y. Yin, "Differentially-fed, wideband dual-polarized filtering antenna with novel feeding structure for 5G sub-6 GHz base station applications," *IEEE Access*, vol. 7, pp. 184718–184725, 2019.

[17] L.-H. Wen *et al.*, "A wideband differentially fed dual-polarized antenna with wideband harmonic suppression," *IEEE Trans. Antennas Propag.*, vol. 67, no. 9, pp. 6176–6181, Sep. 2019.

[18] Q.-X. Chu, Y.-L. Chang, and J.-P. Li, "Crisscross-shaped ±45° dual-polarized antenna with enhanced bandwidth for base stations," *IEEE Trans. Antennas Propag.*, vol. 69, no. 4, pp. 2341–2346, Apr. 2021.

[19] M. Xun, W. Yang, W. Feng, Y. Zhang, Q. Xue, and W. Che, "A differentially fed dual-polarized filtering patch antenna with good stopband suppression," *IEEE Trans. Circuits Syst. II, Exp. Briefs*, vol. 68, no. 4, pp. 1228–1232, Apr. 2021.

[20] Q. Xue, S. W. Liao, and J. H. Xu, "A differentially-driven dual-polarized magneto-electric dipole antenna," *IEEE Trans. Antennas Propag.*, vol. 61, no. 1, pp. 425–430, Jan. 2013.

[21] J.-N. Sun, J.-L. Li, and L. Xia, "A dual-polarized magneto-electric dipole antenna for application to N77/N78 band," *IEEE Access*, vol. 7, pp. 161708–161715, 2019.

[22] J. Y. Yin and L. Zhang, "Design of a dual-polarized magnetoelectric dipole antenna with gain improvement at low elevation angle for a base station," *IEEE Antennas Wireless Propag. Lett.*, vol. 19, no. 5, pp. 756–760, May 2020.

[23] A. Chlavin, "A new antenna feed having equal *E*- and *H*-plane patterns," *Trans. IRE Prof. Group Antennas Propag.*, vol. 2, no. 3, pp. 113–119, Jul. 1954.

[24] K. C. Guapta, R. Garg, I. Bahl, and P. Bhartia, *Microstrip Lines and Slotlines*. Boston, MA, USA: Aretch House, 1996, pp. 292–295.

[25] Y. Chen, W.-J. Lu, L. Zhu, and H.-B. Zhu, "Square loop antenna under even-mode operation: Modelling, validation and implementation," *Int. J. Electron.*, vol. 104, no. 2, pp. 271–285, Feb. 2017.

[26] C. A. Balanis, *Antenna Theory: Analysis and Design*, 3rd ed. New York, NY, USA: Wiley, 2005.

[27] J.-S. Hong, H. Shaman, and Y.-H. Chun, "Dual-mode microstrip open-loop resonators and filters," *IEEE Trans. Microw. Theory Techn.*, vol. 55, no. 8, pp. 1764–1770, Aug. 2007.

Dong Yang was born in Liaoning, China, in 1991. He received the M.S. degree in electromagnetic field and microwave technology from Xidian University, Xi'an, China, in 2018, where he is currently pursuing the Ph.D. degree in electronic science and technology.

His research interests include filtering antenna design, metamaterial, and base station antenna array.

Huiqing Zhai (Member, IEEE) was born in Jilin, China. He received the Ph.D. degree in electromagnetic fields and microwave technology from Xidian University, Xi'an, China, in 2004.

From 2005 to 2008, he was a JSPS Research Fellow with Tohoku University, Sendai, Japan. From 2008 to 2010, he was a Research Fellow with the University of Texas at Arlington, Arlington, TX, USA. Since 2019, he has been the Head of the Microwave Telecommunication Engineering Department, Xidian University, where he is currently a Full Professor and Ph.D. Supervisor. He has authored or coauthored over 100 articles in referred journal and has over ten authorized invention patents. His current research interests include antennas for wireless communication, electromagnetic materials, electromagnetic detection, and electromagnetic invisibility cloaking.

Chaozong Guo was born in Hebei, China, in 1997. He received the bachelor's degree in electronic and information engineering from Xidian University, Xi'an, China, in 2017, where he is currently pursuing the Ph.D. degree in electromagnetic field and microwave technology.

His current research interests include the decoupling of MIMO antennas and electromagnetic metamaterial.

Chang Ma was born in Suzhou, Anhui, China, in 1998. He received the B.S. degree in electronic and information engineering from Xidian University, Xian, China, in 2020, where he is currently pursuing the M.S. degree in electronic science and technology with the School of Electronic Engineering.

His current research interests include absorber frequency selective surface.